W. Zhu, M. Morandini
Nonlinear Smart Beam Model for Energy Harvesting
Journal of Vibration and Acoustics, Vol. 143, N. 5, 2021, 051008 (11 pages)
doi:10.1115/1.4049383

Nonlinear smart beam model for energy harvesting

Wenguo Zhu
School of Aeronautic Science and Engineering
Beihang University
Beijing 100191, People's Republic of China
Email: zhuwenguo@buaa.edu.cn

Marco Morandini*
Dipartimento di Scienze e Tecnologie Aerospaziali
Politecnico di Milano
Milano 20156, Italy
Email: marco.morandini@polimi.it

In this paper, the nonlinear modeling of beam energy harvester embedded with piezoelectric transducers is presented. Starting from a multibody dynamics perspective, a fully coupled electromechanical nonlinear beam model was derived and a geometrically exact finite volume beam element, including the circuit equation is developed. In this model, the beam resultants-strain constitutive law and mass properties are obtained from a 2D beam cross sectional modeling in which the electromechanical coupling effects are included. The results are verified against numerical and experimental results reported in the literature.

Keywords: multiphysics; beam; energy harvesting; nonlinear.

1 Introduction

Flexible and lightweight structures are widely used in industries; this is especially true for beam-like slender structures, such as morphing wings and rotor blades. These structures are known to suffer from mechanical vibrations. The inclusion of smart materials in such structures not only can help suppressing unwanted vibrations, but it can also provide a means to harvest energy from the mechanical vibrations. The harvested energy can thus be used to power low-power electronics on board. Piezoeletric materials do exhibit relatively high electromechanical coupling and are relatively ease to integrate into flexible structures. For these reasons beam structures embedded with piezoelectric devices are the most common structure utilized in vibration-based energy harvesting. An advanced application in aerospace is the multi-functional composite sandwich wing spar of UAVs (Unmanned Aerial Vehicles), in which the wing spar is designed to harvest energy from the wing vibrations by PZT-based harvester, and achieve the wind gust alleviation response simultaneously via vibration control by using PZT actuator, thus realizing a self-contained gust alleviation system [1].

Many pioneering works do study piezoelectric beam energy harvesting systems (PBEHs). Various theoretical model has been proposed. A single degree of freedom (SDOF) lumped parameter model of the PBEHs was used to analyze the system dynamic response [2]; this type of method, however, provide only a rough estimate of the maximum power harvesting and is limited to a single vibration mode, cfr. [3]. Based on Euler-Bernoulli beam theory, a theoretical model of a piezoelectric energy harvesting device was derived in [4] that is based on the energy method and is solved by the Rayleigh-Ritz method. Comprehensive theoretical modeling methods on vibration-based piezoelectric energy harvesting systems and experiments were reviewed in [5]. The spectral finite elements method was developped in [3] to simulate bimorph piezoelectric beam energy harvesters based on the Timoshenko beam theory and on the Euler-Bernoulli beam theory. Although only one element was used in the numerical simulation, considerable correlation is achieved with experiment data. Recently the superconvergent elements method was used to analyze the bimorph beam in [6] and the results were compared with those obtained using an Euler-Bernoulli model and a Timoshenko model. All these papers, however, make use of linear one dimensional beam models; furthermore, the beam stiffness is computed by engineering formulas, which is insufficient to accurately model slender composite beams, such as flexible wings, blades and multi-stable beam based energy harvesters which suffer from large deformations. Recently, The variational asymptotic method (VAM) was used to derive the nonlinear electromechanical model of a rotating beam with embedded piezoelectrics

*CorrespondingAuthor

and an investigation on energy harvesting from helicopter blades was conducted [7]. A multifunctional flexible wing was modeled using a strain-based geometrically nonlinear beam theory in [8]; the electromechanical systems's equation, including the electric circuit equation, was formulated by accounting for the electromechanical effects in the internal virtual work. Based on VAM, a comprehensive smart beam analysis framework was proposed in [9]. In their work, the two dimensional cross sectional analysis tool VABS was utilized to calculate the beam stiffness and electromechanical coupling coefficients; their in-house program NATASHA (Nonlinear aeroelastic trim and stability of HALE aircraft), based on a geometrically exact intrinsic beam theory and a mixed variational principle, was extended to the case of smart beams, allowing the simulation of energy harvesting from beams. A similar beam formulation, also based on a mixed variational principle, was used also in [10, 11] to model the nonlinear dynamics of piezo-composite beams.

This paper, starting from a multibody dynamics perspective, derives a fully coupled electromechanical nonlinear beam model and develops a geometrically exact finite volume beam element, including the circuit equation; this element, needs, as input, the electromechanical cross-section properties of the beam, that can be obtained by following either [12], [13] or [14]. Key points of the proposed formulations are to be completely nonlinear, geometrically exact, intrinsic, and based on a minimal set of nodal unknowns. Departing from e.g. [15, 16] the present formulation does not link the cross-section rotation to the transverse displacement derivative, a choice that would limit the formulation to relatively small rotations; furthermore, the set of nodal unknowns is minimal, without the need to introduce additional generalized strain or force and moment unknowns as in [7–11]. Furthermore, the finite volume beam formulation is free from shear locking [17]. The content is organizes as follows: first the finite volume beam formulation accounting for energy harvesting is derived in detail; then the circuit equation is discretized and linearized to accommodate the multibody dynamics solving procedure; and finally the numerical example is carried out.

2 Beam theory

This paper modifies a geometrically exact beam element proposed in [17], that is based on the finite volume method. The beam element intrinsically accounts for shear deformation and is free from shear locking. It is here extended to allow fully-coupled electromechanical simulations of beams made with piezoelectric patches.

2.1 Equilibrium equation

The beam is represented by a reference line, with local arc length ξ, and a reference cross section which is perpendicular to the undeformed reference line. The equilibrium equation can be written as

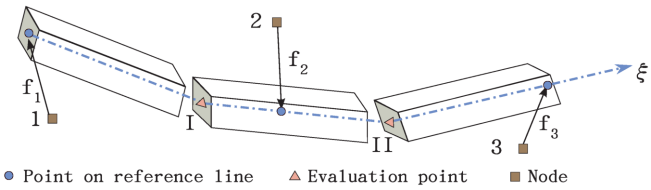

Fig. 1: Three-node finite volume beam

$$\boldsymbol{\vartheta}' - \boldsymbol{T}\boldsymbol{\vartheta} + \boldsymbol{\tau} = \boldsymbol{0} \tag{1}$$

where $\boldsymbol{\vartheta} = \begin{Bmatrix} \boldsymbol{t} \\ \boldsymbol{m} \end{Bmatrix}$ is a vector stacking the internal force and moment, $\boldsymbol{T} = \begin{bmatrix} \boldsymbol{0} & \boldsymbol{p}'\times \\ \boldsymbol{0} & \boldsymbol{0} \end{bmatrix}$, $\boldsymbol{p}(\xi)$ is the position vector of arbitrary point at the beam reference line location ξ in global reference frame, $(\cdot)'$ denotes the derivative with respect to ξ, $(\cdot)\times$ denotes the skew symmetric matrix corresponding to the vector, and $\boldsymbol{\tau}$ is the imposed load vector including the inertial forces. A weak form of Eqn. (1) can be written as

$$\int_a^b w(\xi)(\boldsymbol{\vartheta}' - \boldsymbol{T}\boldsymbol{\vartheta} + \boldsymbol{\tau})\mathrm{d}\xi = \boldsymbol{0}, \tag{2}$$

with $w(\xi)$ a suitable test function. By using a piecewise constant discontinuous test function $w(\xi) = step(\xi - a) - step(\xi - b)$, which has unit value inside the domain $[a,b]$ and is equal to zero outside this domain, yields

$$\left(\boldsymbol{I} - \boldsymbol{U}^T(\xi)\right)\boldsymbol{\vartheta}\big|_a^b = -\int_a^b w(\boldsymbol{I} - \boldsymbol{U}^T(\xi) + \boldsymbol{U}^T(\xi_0))\boldsymbol{\tau}\mathrm{d}\xi \tag{3}$$

where ξ_0 is a point with respect to which the moment is referred to, $\boldsymbol{I}$ is the identity matrix, and $\boldsymbol{U}(\xi) = \int \boldsymbol{T}\mathrm{d}\xi$ refers to the moment arms of the internal and external forces.

The two points located at Gauss integration points are used as evaluation points to evaluate the internal forces; thus the beam element is splitted into three volumes denoted by the end points $V_{1\to I}$, $V_{I\to II}$ and $V_{II\to 3}$, as depicted in Figure 1. Applying Eqn. (3) to the above finite volumes , and taking node 1, 2, 3 as moment reference point ξ_0 respectively, yields the equilibrium equations at the three nodes as follows:

$$\boldsymbol{L}\boldsymbol{\Theta} = \boldsymbol{F} \tag{4}$$

$$\boldsymbol{\Theta} = \boldsymbol{Z}\tilde{\boldsymbol{\Theta}} \tag{5}$$

where

$$\boldsymbol{L}=\begin{bmatrix} -\boldsymbol{I} & \boldsymbol{0} & \boldsymbol{0} & \boldsymbol{0} \\ (\boldsymbol{p}_I-\boldsymbol{x}_1)\times & -\boldsymbol{I} & \boldsymbol{0} & \boldsymbol{0} \\ \boldsymbol{I} & \boldsymbol{0} & -\boldsymbol{I} & \boldsymbol{0} \\ -(\boldsymbol{p}_I-\boldsymbol{x}_2)\times & \boldsymbol{I} & (\boldsymbol{p}_{II}-\boldsymbol{x}_2)\times & -\boldsymbol{I} \\ \boldsymbol{0} & \boldsymbol{0} & \boldsymbol{I} & \boldsymbol{0} \\ \boldsymbol{0} & \boldsymbol{0} & (\boldsymbol{p}_{II}-\boldsymbol{x}_3)\times & \boldsymbol{I} \end{bmatrix} \tag{6}$$

is the moment arm matrix, $\boldsymbol{p}_\alpha(\alpha=I, II)$ is the position vector of the evaluation point, and $\boldsymbol{x}_i(i=1, 2, 3)$ is the position vector of the node in global frame. Here $\tilde{\boldsymbol{\Theta}}$ is a 12×1 vector, stacked by the internal force vectors at points *I* and *II* in material frame, and $\boldsymbol{\Theta}$ is its counterpart in the global frame. The internal force at points *I* and *II* can be calculated by using the generalized constitutive law discussed in Section 2.2. Matrix $\boldsymbol{Z}=\mathrm{diag}(\boldsymbol{R}_I, \boldsymbol{R}_I, \boldsymbol{R}_{II}, \boldsymbol{R}_{II})$, and $\boldsymbol{R}_\alpha(\alpha=I, II)$ is the transformation matrix from material frame to global frame at points *I* and *II*. The 18×1 vector $\boldsymbol{F}$ is the imposed nodal force vector at the three nodes, accounting also for the inertial forces in global frame.

2.2 Generalized beam deformation

The measures of beam linear strain and angular curvature difference in global frame can be defined as

$$\boldsymbol{\varepsilon}=\boldsymbol{p}'-\boldsymbol{R}\tilde{\boldsymbol{p}}_0' \tag{7}$$

$$\boldsymbol{\kappa}\times=\boldsymbol{R}'\boldsymbol{R}^T-\boldsymbol{R}\tilde{\boldsymbol{\rho}}_0\times\boldsymbol{R}^T \tag{8}$$

where $\boldsymbol{R}$ is the rotation tensor identifying the beam cross-section orientation, the quantities with subscript $(\cdot)_0$ denote the initial value of entities, $\tilde{\boldsymbol{p}}_0=\boldsymbol{R}_0^T\boldsymbol{p}_0'$, $\tilde{\boldsymbol{\rho}}_0$ is the initial curvature vector in the reference configuration material frame, $\tilde{\boldsymbol{\rho}}_0\times=\boldsymbol{R}_0^T\boldsymbol{R}_0'$, $\boldsymbol{\varepsilon}$ is the beam strain measure and $\boldsymbol{\kappa}$ is the elastic curvature vector. Since the material constitutive law does not depend on configurations when expressed in material frame, the internal force and moment are firstly evaluated in material frame and then transformed into current frame of each point. The strain measures defined in Eqn. (7) and (8) can be transformed into material frame

$$\tilde{\boldsymbol{\varepsilon}}=\boldsymbol{R}^T\boldsymbol{p}'-\tilde{\boldsymbol{p}}_0' \tag{9}$$

$$\tilde{\boldsymbol{\kappa}}\times=\boldsymbol{R}^T\boldsymbol{\rho}\times\boldsymbol{R}-\tilde{\boldsymbol{\rho}}_0\times \tag{10}$$

where $\tilde{(\cdot)}$ denote the entities expressed in material frame and $\boldsymbol{\rho}\times=\boldsymbol{R}'\boldsymbol{R}^T$. The strain rate in material frame can be expressed as:

$$\dot{\tilde{\boldsymbol{\varepsilon}}}=\boldsymbol{R}^T(\dot{\boldsymbol{l}}-\boldsymbol{\omega}\times\boldsymbol{l}) \tag{11}$$

$$\dot{\tilde{\boldsymbol{\kappa}}}=\boldsymbol{R}^T(\dot{\boldsymbol{\rho}}-\boldsymbol{\omega}\times\boldsymbol{\rho}) \tag{12}$$

$$\boldsymbol{l}=\boldsymbol{p}' \tag{13}$$

$$\dot{\boldsymbol{l}}=\dot{\boldsymbol{p}}' \tag{14}$$

$$\dot{\boldsymbol{\rho}}=\boldsymbol{\omega}'+\boldsymbol{\omega}\times\boldsymbol{\rho} \tag{15}$$

where $\boldsymbol{l}=\boldsymbol{p}'$ is the derivative of the position of point on reference line with respect to abscissa ξ, which describes how the line strains in space and $\boldsymbol{\omega}$ is the angular velocity of the section.

Following the semi-analytical approach proposed by e.g. [14, 18], the internal resultants can be related to the beam generalized deformations by means of a linear constitutive law in material frame

$$\begin{bmatrix} \tilde{\boldsymbol{t}} \\ \tilde{\boldsymbol{m}} \\ \boldsymbol{q} \end{bmatrix}=\begin{bmatrix} \boldsymbol{A} & \boldsymbol{B} & -\boldsymbol{K}_\varepsilon^T \\ \boldsymbol{B}^T & \boldsymbol{D} & -\boldsymbol{K}_\kappa^T \\ \boldsymbol{K}_\varepsilon & \boldsymbol{K}_\kappa & \boldsymbol{C}_p \end{bmatrix}\begin{bmatrix} \tilde{\boldsymbol{\varepsilon}} \\ \tilde{\boldsymbol{\kappa}} \\ \boldsymbol{V} \end{bmatrix} \tag{16}$$

or, in a compact form,

$$\tilde{\boldsymbol{\vartheta}}=\tilde{\boldsymbol{S}}\tilde{\boldsymbol{\psi}}, \tag{17}$$

where $\tilde{\boldsymbol{t}}$ represents the internal force resultant, $\tilde{\boldsymbol{m}}$ the internal moment resultant in material frame, $\boldsymbol{q}$ is the electric charge per unit length, $\boldsymbol{A}$, $\boldsymbol{B}$ and $\boldsymbol{D}$ are blocks of stiffness matrix, $\boldsymbol{K}_\varepsilon$ and $\boldsymbol{K}_\kappa$ are electromechanical coupling coefficients corresponding to elastic strains and curvatures respectively, and $\boldsymbol{C}_p$ is the electric capacitance matrix, $\boldsymbol{V}$ is the electric voltage difference vector on the electrode pairs. $\tilde{\boldsymbol{\vartheta}}$ is the sectional resultants vector in material frame, $\tilde{\boldsymbol{S}}$ is the sectional constitutive law, and $\tilde{\boldsymbol{\psi}}$ is the generalized beam deformation vector in material frame.

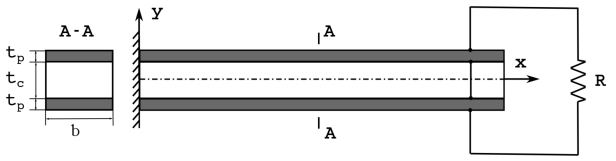

Fig. 2: A cantilever bimorph piezoelectric energy harvester

2.3 Circuit equation

Assume that the whole beam is covered by the piezoelectric layers, with continuous electrodes. If the electrode is not continuous then the following equations are meant to be satisfied for each portion of the beam with an independent pair of electrodes. The electric charge of the beam is thus equal to

$$\boldsymbol{Q} = \int_0^L \boldsymbol{q}\mathrm{d}l \tag{18}$$

where L is the beam length. The electric current entering the beam is equal to the time derivative of the charge:

$$\dot{\boldsymbol{Q}} = \int_0^L (\boldsymbol{K}_\varepsilon\dot{\tilde{\boldsymbol{\varepsilon}}} + \boldsymbol{K}_\kappa\dot{\tilde{\boldsymbol{\kappa}}} + \boldsymbol{C}_p\dot{\boldsymbol{V}})\mathrm{d}l \tag{19}$$

The first two terms of Eqn. 19 represent the electromechanical coupling contribution; the third term is due to the electric capacitance of piezoelectric materials. The current due to the external resistance R_l can be calculated by $I_r = \frac{V_p}{R_l}$, and V_p is the voltage applied on resistance, for the bimorph beam, V_p is the voltage difference on the two electrodes. For the typical electric circuit of energy harvesting, as shown in Figure 2, according to the Kirchhoff's first law, the sum of currents flowing into the electric node is equal to the sum of currents flowing out of that node, the electrical equation can be formulated as

$$\int_0^L (\boldsymbol{K}_\varepsilon\dot{\tilde{\boldsymbol{\varepsilon}}} + \boldsymbol{K}_\kappa\dot{\tilde{\boldsymbol{\kappa}}} + \boldsymbol{C}_p\dot{\boldsymbol{V}})\mathrm{d}l = -\frac{V_p}{R_l} \tag{20}$$

Combining Eqn. (4) and Eqn. (20) leads to the fully coupled electromechanical equation of piezoelectric beam

$$\begin{aligned} \boldsymbol{L\Theta} &= \boldsymbol{F} \\ \int_0^L (\boldsymbol{K}_\varepsilon\dot{\tilde{\boldsymbol{\varepsilon}}} + \boldsymbol{K}_\kappa\dot{\tilde{\boldsymbol{\kappa}}} + \boldsymbol{C}_p\dot{\boldsymbol{V}})\mathrm{d}l &= -\frac{V_p}{R_l} \end{aligned} \tag{21}$$

Equation (21) will be discretized in space, and integrated in time domain using a implicit A/L stable linear multistep integration scheme, proposed by [19, 20], also reported in Appendix A for completeness.

3 Circuit equation discretization

The original unknowns of governing Eqn. (21) are the position $\boldsymbol{p}$ and rotation matrix $\boldsymbol{R}$ of points on reference line. The Cayley-Gibbs-Rodrigues (CRG) rotation parameter $\boldsymbol{g}$ is used to represent the rotations; a few details about the rotation treatment are reported in Appendix B. The position and the rotation parameter of an arbitrary point on the beam reference line can be interpolated from the nodal values by using a parabolic shape function:

$$\boldsymbol{p}(\xi) = N_i(\xi)(\boldsymbol{x}_i + \boldsymbol{R}_i f_{i0}) \tag{22}$$

$$\boldsymbol{g}(\xi) = N_i(\xi)\boldsymbol{g}_i \tag{23}$$

where $\boldsymbol{R}_i$ is the rotation matrix of node i, and $\boldsymbol{f}_{i0}$ is the initial configuration beam reference line offset at node i . Since the piezoelectric patches cover the entire beam span, the voltage on the same electrode of each beam element keeps same. Thus we have

$$\boldsymbol{V} = [\,1\ 1\ \ldots\ 1\,]^T_{1\times N} V_p \tag{24}$$

The discretized form of generalized strains is:

$$\boldsymbol{\varepsilon}(\xi) = N_i'(\xi)(\boldsymbol{x}_i + \boldsymbol{R}_i\boldsymbol{f}_{i0}) - \boldsymbol{R}(\xi)\tilde{\boldsymbol{p}}' \tag{25}$$

$$\boldsymbol{\kappa}(\xi) = \boldsymbol{G}(\xi)N_i'(\xi)\boldsymbol{g}_i + \boldsymbol{R}_\delta(\xi)\boldsymbol{\kappa}_r \tag{26}$$

where $\boldsymbol{R}_\delta$ is the variation of rotation matrix from the predicted one at the beginning of the current time step, see Appendix B for details.

Note that Eqn. (20) involves an integration along the beam span, and that the integral is nothing but the sum of charges on each element. At each element, the same two Gauss evaluation points of the three node beam element, located at $\pm\frac{1}{\sqrt{3}}$ of the element axis, are used in order to approximate the integral over an element. The summation over all the elements is implicitly performed during the assembling process of the global Jacobian matrix and residual vector since different beam elements are linked to the same electric node. The discretized circuit equation at element level can thus be written as:

$$\sum \boldsymbol{J} w_\alpha(\boldsymbol{K}_\varepsilon\dot{\tilde{\boldsymbol{\varepsilon}}}_\alpha + \boldsymbol{K}_\kappa\dot{\tilde{\boldsymbol{\kappa}}}_\alpha + \boldsymbol{C}_p\dot{\boldsymbol{V}}_\alpha) = -\frac{V_p}{R_l}, \tag{27}$$

where $\boldsymbol{J}$ is the discretization Jacobian matrix and $w_\alpha(\alpha{=}I, II)$ is the weight coefficient for second order Gauss quadrature, $w_I = w_{II} = 1$. The curvature time derivative $\dot{\boldsymbol{\kappa}}$ is computed as $\dot{\hat{\boldsymbol{\kappa}}} \approx \boldsymbol{R}^T(\boldsymbol{G}(\xi)N_i'(\xi)\dot{\boldsymbol{g}} + \dot{\boldsymbol{G}}(\xi)N_i'(\xi)\boldsymbol{g}_i - \boldsymbol{\omega}\times(\boldsymbol{G}(\xi)N_i'(\xi)\boldsymbol{g}_i)) + \dot{\kappa}_r$.

To solve the system, the equations needs to be linearized with respect to the system unknowns, i.e. the nodal position $\boldsymbol{x}$ and rotation parameters $\boldsymbol{g}$. Explicit expressions for the linearization are reported, for completeness, in Appendix C.

4 Numerical validation

The proposed formulation is validated by following numerical examples.

4.1 Bimorph cantilever beam

A bimorph piezoelectric cantilever beam manufactured by Piezo System Inc is studied, which has already been considered by [5]. The velocity at beam tip and voltage drop across the resistance load under the different excitation frequencies and various resistance loads are studied.

The beam is of length 24.53 mm, and composited by three layer, with a brass core base layer and two PZT-5H layers on the top and bottom. The beam cross section is as depicted in Figure 2, is 6.4 mm wide. The brass layer is 0.14 mm thick with Young's modulus of 105 GPa, density of 9000 kg/m^3, and a Poison ratio 0.33 was assumed during the simulation. The two piezoelectric layers have the same thickness of 0.265 mm and the Strain-Charge form properties of PZT-5H are listed in Table 1. Here the three dimensional properties of PZT-5H were used rather than reduce properties adopted by engineering beam models in [3, 5]. In the experiment of [5], the bimorph beam was excited at the clamped root by an electromagnetic shaker, and the velocity was measured at 1.5 mm from the free end.

In the simulation, the cross sectional are first computed by leveraging the semi-analytical procedure proposed by [14], that is based on the solution of the de Saint-Venant problem. The procedure can deal with beam cross-sections with arbitrary geometry and materials using triangular or quadrilateral elements, and a fully electromechanically coupled stiffness matrix and inertial matrix are obtained. Table 2 shows the nonzero stiffness coefficients of the 8×8 stiffness matrix of the cross section. A_{11}, A_{22}, and A_{33} are the extension stiffness, the transversal shear stiffness. D_{11}, D_{22} and D_{33} are the torsional stiffness and the two bending stiffness, respectively. $K_{\varepsilon 13}$, $K_{\varepsilon 23}$ are extension and electric load coupling coefficient due to the top and bottom piezoelectric layer respectively, and $K_{\kappa 12}$, $K_{\kappa 22}$ are the bending and electric load coupling coefficient due to the top and bottom piezoelectric layer respectively. The beam is represented by using 20 three-nodes finite volume beam elements. The viscous damping ratio of 0.874% of the first order of vibration frequency identified by [5] is reproduced by an equivalent damping of 5.1693×10^{-6} s/rad proportional to the beam stiffness.

The present numerical model is solved in the time domain, and its eigenvalues of the system are computed by performing a direct eigeanalysis of the linearized equation [21]. Table 3 lists the fundamental frequencies of the energy harvester beam under the short-circuit (R=470 Ω) and open-circuit (R=995 kΩ) condition. The slight differences with respect to [3] predicted frequencies are due to the fact that Wang assumes, just like [5] an axial state of stress for the beam, while the present approach computes the beam cross-section stiffness matrix accounting for the complete three dimensional stress state; since the Poisson coefficients of the piezoelectric and passive material are different, and the active beam portion is made by gluing together relatively thin layers, the transverse stress due to an axial load or to bending is not exactly equal to zero, and accounts for a slightly higher axial and bending stiffness, thus for the slightly higher predicted bending frequencies. Figure 3-6 show, for different excitation frequencies and an excitation amplitude equal to one g, the velocity of beam tip, at 1.5 mm from the free end, and the voltage drop across the resistance load; different external resistance loads are considered: $R = 470\,\Omega$ (short circuit), $R = 1.2\,\text{k}\Omega$, $R = 44.9\,\text{k}\Omega$, and $R = 995\,\text{k}\Omega$ (open circuit).

Experimental data from [5] and theoretical results from [3] are used to validate the present method. Figure 3-6 suggest that the present method achieves a good coincidence with the experiment both for mechanical and electrical responses. Figure 7 shows the frequency responses of the power and current under various resistance loads. It can be seen that as the resistance load increases, both the fundamental frequency of the bimorph beam and the voltage increase, while the current decreases for higher resistance loads. Figure (7a) shows that the maximum power is harvested for a resistance load of $R = 9.9\,\text{k}\Omega$.

4.2 Three-layer smart beam

A three layered beam which has been studied in literature [11] by using VABS and SGEBT (Smart Geometrically Exact Beam Theory) is investigated to validate the present method. The substrate of the beam is made of T300/934 fiber composite; a piezoelectric layer is bounded to the top of the substrate by an adhesive layer. The beam is 1 m long, has a large aspect ratio of 39.37, and the cross section geometry is depicted in Figure 8. The material properties, taken from [11], are reported in Table 4. In the work of [11], the smart beam was discretized by 20 beam elements, and each beam element was modeled as an independent sensor; in other word, the top surface of piezoelectric layer is made of 20 segmented electrodes rather than one continuous electrode. As a comparison, both linear and nonlinear 3D FEM analysis were also run by using Abaqus in [11]. Both of the simulations are carried out under the open circuit condition.

Table 1: Material properties of PZT-5H(www.efunda.com)

Properties	PZT-5H	Properties	PZT-5H
$s^E{}_{11} = s^E{}_{22}$ ($\times 10^{-12}$ m^2/N)	16.5	$d_{31} = d_{32}$ ($\times 10^{-12}$ C/N)	-274
$s^E{}_{12}$ ($\times 10^{-12}$ m^2/N)	-4.78	d_{33} ($\times 10^{-12}$ C/N)	593
$s^E{}_{13}$ ($\times 10^{-12}$ m^2/N)	-8.45	$d_{15} = d_{24}$ ($\times 10^{-12}$ C/N)	741
$s^E{}_{33}$ ($\times 10^{-12}$ m^2/N)	20.7	$\varepsilon^T_{11}/\varepsilon_0 = \varepsilon_{22}/\varepsilon_0$	3130
$s^E{}_{44} = s^E{}_{55}$ ($\times 10^{-12}$ m^2/N)	43.5	$\varepsilon_{33}/\varepsilon_0$	3400
$s^E{}_{66}$ ($\times 10^{-12}$ m^2/N)	42.6	ε_0 ($\times 10^{-12}$ F/m)	8.854
ρ (kg/m^3)	7500		

Table 2: Stiffness and mass properties of cross section

Properties	Value
A_{11} (N)	3.00×10^5
A_{22} (N)	9.63×10^4
A_{33} (N)	1.81×10^4
D_{11} (Nm^2)	1.42×10^{-2}
D_{22} (Nm^2)	1.01×10^{-2}
D_{33} (Nm^2)	1.02×10^0
$K_{\varepsilon 13} = K_{\varepsilon 23}$ (Cm)	1.04×10^{-1}
$K_{\kappa 12} = -K_{\kappa 22}$ (C)	2.04×10^{-5}
$C_{p11} = C_{p22}$ (Fm^{-1})	5.69×10^{-7}
$C_{p12} = C_{p21}$ (Fm^{-1})	-1.22×10^{-8}

In the following figures and tables, the notations Abaqus Linear, Abaqus and SGEBT denote the results obtained in [11] and computed by linear and nonlinear 3D FEM analysis in Abaqus, and SGEBT respectively.

The 2D cross section analysis is performed firstly. As shown in Figure 8, the cross section is meshed by 5000 triangle elements using Gmsh [22]. The interface between adhesive layer and piezoelectric layer is grounded. The nonzero stiffness matrix terms are listed in Table 5, and are compared with those from [11] which are computed by VABS. It can be seen that a good correlation exists between the present results and those reported by [11] except for the capacitance which shows a relative difference of 2.97%.

In order to keep consistency with [11], the same number of beam elements are used in present study, and an external resistance of 10^8 Ω is connected to each beam element to mimic the open circuit condition. A direct eigenanalysis is performed and the first five vertical bending frequencies are listed in Table 6. Compared with results from [11] both calculated by SGEBT and Abaqus, it can be seen that the present model predicted the natural frequencies accurately. A vertical sinusoidal dead load $F = 10^3 \sin(2\pi ft)$ N, $f = 19$ Hz, which is close to the fundamental bending frequency, is then applied at the tip of the smart beam. The time response of the tip vertical displacement and the voltage harvested at the root element are computed and compared with the results from [11] in Figure 9 and Figure 10. It can be observed that present method predicts both the mechanical response and electrical response accurately, and the results computed by present method is much closer to the 3D FEM results than those of SGEBT.

Note that the maximum tip deflection reaches about 0.9 m, 90% of the beam span. The beam is definitely geometrically nonlinear, and suffers large rotation and deformation. The present method is capable to capture the nonlinear behavior accurately. In addition, according to the reported time consumption of SGEBT and Abaqus in [11], the nonlinear transient 3D FEM analysis in Abaqus costs 562786.00 s (6.51 days) and SGEBT costs 9596.89 s on a platform with configuration of 64-bit, Intel® Xeon® CPU E3-1241 v3 @ 3.50 GHz, 32 GB RAM. However, by using the present method, only 272.5 s are required (55.6 s for cross section analysis, 216.9 s for nonlinear beam analysis with a time step of 0.0001 s) when executed on a desktop computer with Intel® Core™ i7-8559U CPU @ 2.70GHz, 32 GB RAM, running a 64-bit Ubuntu distribution. The computational time is remarkably reduced compared to 3D FEM analysis, still achieving an acceptable accuracy.

The responses under the dead load are also compared with results computed by linear analysis in Abaqus from [11]; as shown in Figure 11 and Figure 12, the linear analysis fails to capture the realistic deformation and generates a nonphysical vertical displacement that greater than the beam length and whose maximum increase with time.

The dynamic response of smart beam under a follower load is also investigated. A sinusoidal follower force with magnitude of 5000 N and period of 0.3142 s is applied at the tip of the above smart beam. As depicted in Figure 13-Figure 15, the time response of axis displacement, vertical displacement at the tip and the voltage measured at the root

Table 3: Fundamental frequency of the bimorph beam

	Experiment [5]	Ref [3]	Present
short-circuit R=470 Ω (Hz)	502.5	507.8	509.3
open-circuit R=995 kΩ (Hz)	524.7	528.3	530.1

Table 4: Material properties

Properties	T300/934	Adhesive	PZT-4
$E_{11} = E_{22}$ (GPa)	126	6.9	68.9
E_{33} (GPa)	7.9	6.9	48.3
$G_{12} = G_{13} = G_{23}$ (GPa)	27.6	2.459	31.0
$\nu_{12} = \nu_{13} = \nu_{23}$	0.275	0.4	0.25
$e_{31} = e_{32}$ (Cm^{-2})	0	0	-7.99
e_{33} (Cm^{-2})	0	0	14.86
ε_{11} (Fm^{-1})	3.089×10^{-11}	5.429×10^{-9}	5.429×10^{-9}
ε_{22} (Fm^{-1})	2.560×10^{-11}	5.429×10^{-9}	5.429×10^{-9}
ε_{33} (Fm^{-1})	2.560×10^{-11}	5.320×10^{-9}	5.320×10^{-9}
Thickness (mm)	15.24	0.254	1.524
Width (mm)	25.4	25.4	25.4

Table 5: Cross section stiffness of the three-layer beam

Properties	VABS	Present
A_{11} (N)	5.149×10^{7}	5.149×10^{7}
A_{22} (N)	9.872×10^{6}	9.874×10^{6}
A_{33} (N)	9.423×10^{6}	9.425×10^{6}
B_{12} (Nm)	-2.238×10^{4}	-2.238×10^{4}
B_{21} (Nm)	-1.421×10^{3}	-1.422×10^{3}
D_{11} (Nm^2)	6.671×10^{2}	6.673×10^{2}
D_{22} (Nm^2)	1.145×10^{3}	1.145×10^{3}
D_{33} (Nm^2)	2.768×10^{3}	2.768×10^{3}
$K_{\varepsilon1}$ (Cm)	-2.430×10^{0}	-2.430×10^{0}
$K_{\kappa2}$ (C)	1.881×10^{-2}	1.882×10^{-2}
C_p (Fm^{-1})	1.840×10^{-7}	1.787×10^{-7}

is compared with the results obtained by nonlinear 3D FEM analysis in Abaqus and SGEBT; the results show a considerable agreement.

4.3 Bistable vertical beam energy harvester

From Section 4.1 it can be seen that the energy harvesting efficiency is dramatically reduced when the excitation frequency departs away from the natural frequency. In order to maximize the harvested energy from a wide range of vibration frequency many innovative energy harvester configurations have been proposed, such as the piezomagnetoelastic energy harvester [5], bistable beams [15, 16, 23] and bistable plates [5, 24]. These devices make use of the nonlinear response of the structure, which have two or three equilibrium positions. In this section, a bistable bulked vertical beam configuration is studied. The beam near bulking configuration undergoes large deformation and presents a markedly nonlinear dynamic response. Since the present beam model is geometrically exact and intrinsically nonlinear, it is a good choice for the simulation of such a problem.

The beam is a vertical cantilever of length L=200 mm, and mounted with a tip mass on the free end, as shown in Figure 16. The beam is made of steel of 0.1 mm thick, and two PZT-5H layers of length L_p=40 mm are mounted on the top and bottom at the clamped root with a thickness of 0.254 mm each . Both the beam and the piezoelectric patches are 16 mm wide. An additional mass of 2.65 g is attached at the tip of the beam. The electrodes are connected serial, and the resistance load is $R = 1000$ kΩ.

The base is excited in the transversal direction by a harmonic excitation $z = z_0 \sin(\omega t)$. The initial condition is

Table 6: Vertical bending natural frequencies under the open circuit condition

Frequency (Hz)	Abaqus	SGEBT	Difference	Present	Difference
1	20.114	20.10	0.0696%	20.097	0.0845%
2	125.78	124.39	1.1051%	125.659	0.0962%
3	351.01	349.25	0.5014%	350.774	0.0672%
4	684.51	685.75	0.1812%	684.561	0.0075%
5	1124.5	1136.11	1.0325%	1125.94	0.1281%

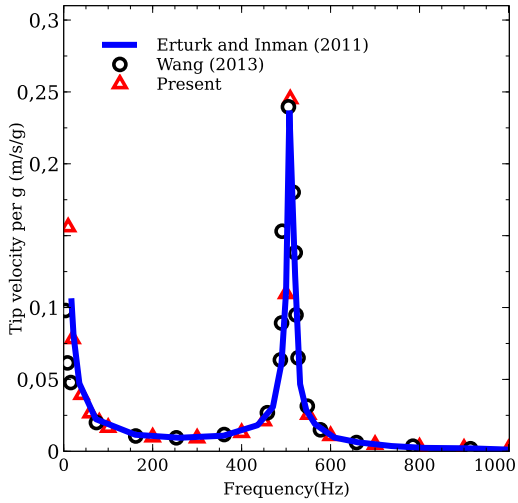

(a) Tip velocity frequency response

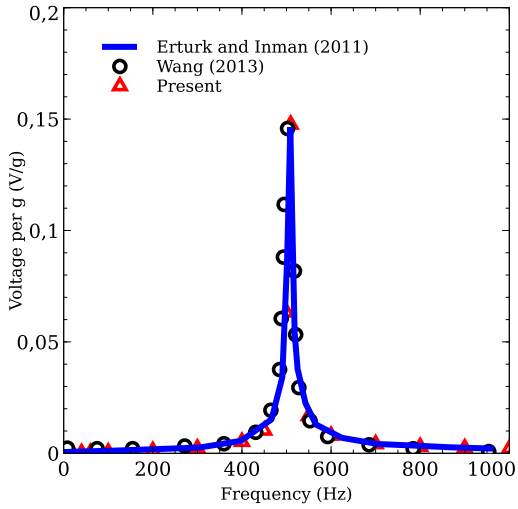

(b) Voltage frequency response

Fig. 3: FRFs of beam tip velocity and voltage, R=470Ω

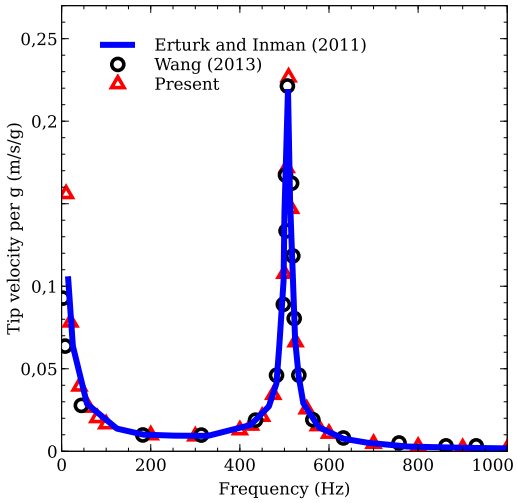

(a) Tip velocity frequency response

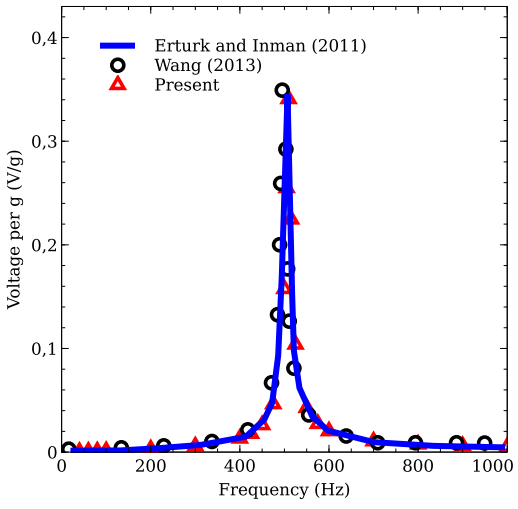

(b) Voltage frequency response

Fig. 4: FRFs of beam tip velocity and voltage, R=1.2 kΩ

$z = 0$ and $\dot{z} = 0$. The first natural frequency of the beam is of about 1.28 Hz. First, a low amplitude excitation with $z_0 = 18.5$ mm, $f = 1.40$ Hz, is applied. Figure 17 shows the transversal displacement, phase trajectory of the tip point of the beam and open-circuit voltage responses. It can be seen that the response is chaotic: the tip point sometimes oscillates around one of the stable buckled position, and sometimes exhibits large oscillations between the two extreme positions. As it can also be seen from Figure 17c the trajectory is oscillating between two potential wells. When the trajectory is transitioning from one bulked equilibrium position to the other, the higher electric power is harvested. The responses under the same amplitude at frequencies of 0.5 Hz, 1.0 Hz, 1.4 Hz and 2.0 Hz are studied, and the Root Mean

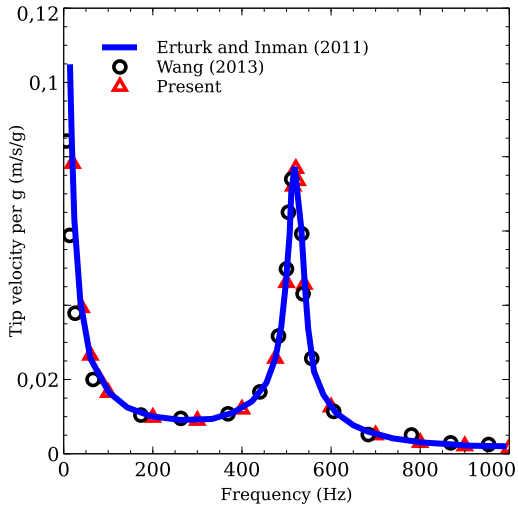

(a) Tip velocity frequency response

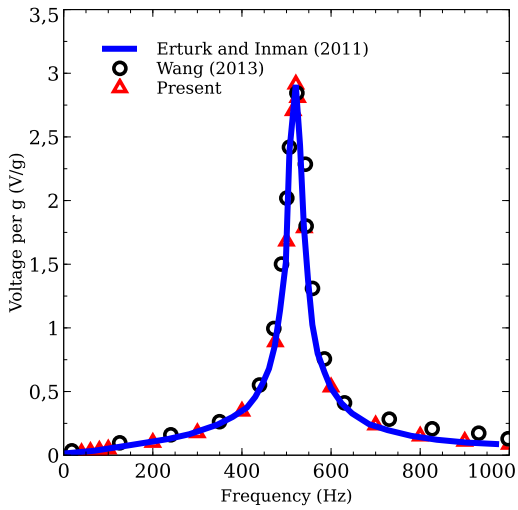

(b) Voltage frequency response

Fig. 5: FRFs of beam tip velocity and voltage, R=44.9 kΩ

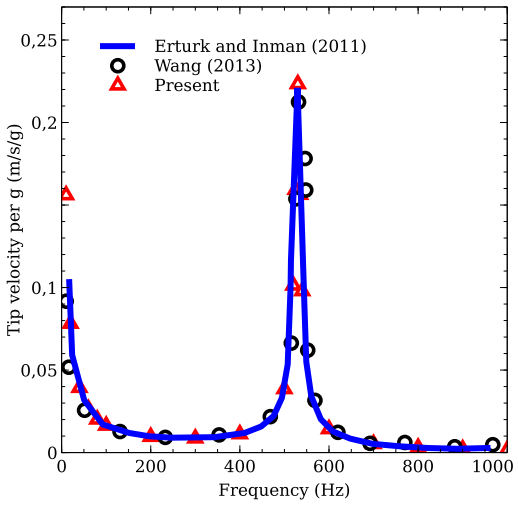

(a) Tip velocity frequency response

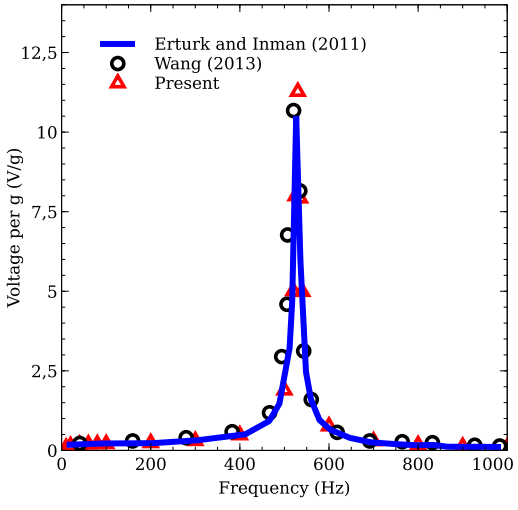

(b) Voltage frequency response

Fig. 6: FRFs of beam tip velocity and voltage, R=995 kΩ

Square (RMS) output voltages at these frequencies, computed after the first 40 s to get rid of initial transient effects, are equal to 1.34 V, 0.58 V, 0.74 V, and 1.86 V respectively. For comparison, the RMS voltages for the same beam but without accounting for gravity, thus without any instability, are equal to 0.16 V, 0.84 V, 2.84 V and 0.89 V, respectively, with a maximum resonance voltage of 4.4 V, see Figure 18. This confirms that the bistable beam is able to extract more energy when the forcing frequency differs from the beam bending frequency, at the expense of a reduced harversting efficiency at resonance.

5 Conclusions

In this paper, a finite volume beam theory is extended to fully coupled electromechanical beam energy harvester within a multibody dynamics framework. It provides a generalized procedure to analysis smart beams. A semi-analytical approach is utilized to compute the beam cross sectional stiffness, electromechanical coupling coefficients and mass inertial properties. By taking these as known the fully couple electromechanical beam analysis is carried out, and the mechanical and electrical response of complex beam systems can be investigated. Although only configurations with simple cross section are studied in this paper, the proposed beam model is capable to model smart beams with arbitrary geometry and arbitrary material. Furthermore, the proposed method can be coupled with aerodynamics codes to study the energy harvesting from aeroelastic vibration.

Acknowledgements

The first author would like to thank the financial support from China Scholarship Council (CSC, NO. 201806020058).

References

[1] Wang, Y., and Inman, D. J., 2013. "Simultaneous energy harvesting and gust alleviation for a multifunctional composite wing spar using reduced energy con-

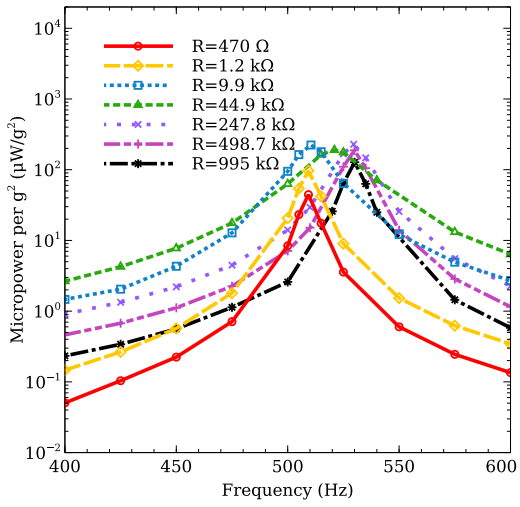

(a) Power

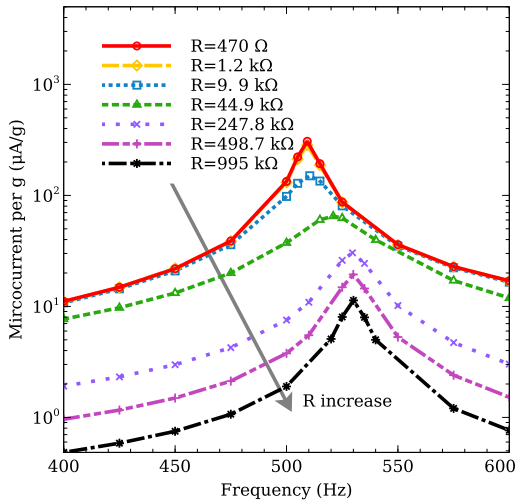

(b) Current

Fig. 7: Electric frequency response under various resistance loads: power and current

Fig. 8: 2D Mesh generated by Gmsh for cross section analysis of three-layer beam

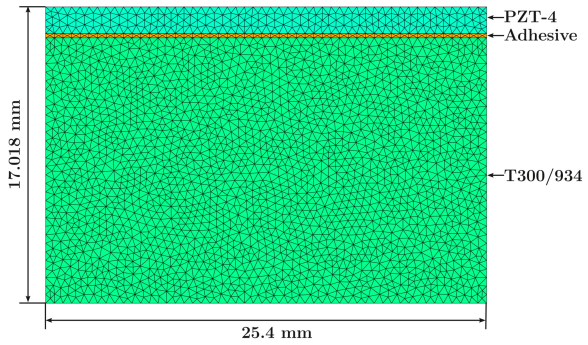

Fig. 9: Vertical displacement at the tip under dead load

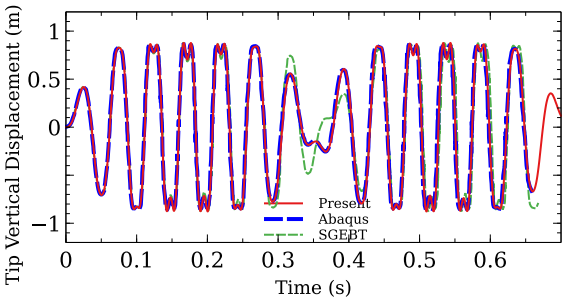

Fig. 10: Voltage harvested at the root element under dead load

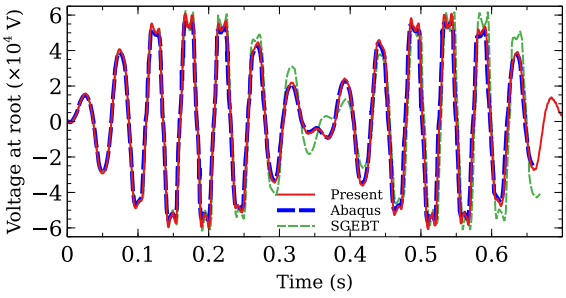

trol via piezoceramics". *Journal of Composite Materials,* **47**(1), pp. 125–146.

[2] Roundy, S., and Wright, P. K., 2004. "A piezoelectric vibration based generator for wireless electronics". *Smart Materials and structures,* **13**(5), p. 1131.

[3] Wang, G., 2013. "Analysis of bimorph piezoelectric beam energy harvesters using timoshenko and euler–bernoulli beam theory". *Journal of Intelligent Material Systems and Structures,* **24**(2), pp. 226–239.

[4] Sodano, H. A., Park, G., and Inman, D., 2004. "Estimation of electric charge output for piezoelectric energy harvesting". *Strain,* **40**(2), pp. 49–58.

[5] Erturk, A., and Inman, D. J., 2011. *Piezoelectric energy harvesting*. John Wiley & Sons.

[6] Hajheidari, P., Stiharu, I., and Bhat, R., 2019. "Analysis of bimorph piezoelectric beam energy harvesters using superconvergent element". *Journal of Intelligent Material Systems and Structures,* **30**(15), pp. 2299–2313.

[7] Vieira, W., Nitzsche, F., and De Marqui Jr, C., 2012. "Modeling and analysis of piezoelectric energy harvesting from helicopter blades". In 53rd AIAA/ASME/ASCE/AHS/ASC Structures, Structural Dynamics and Materials Conference 20th AIAA/ASME/AHS Adaptive Structures Conference 14th AIAA, p. 1665.

[8] Tsushima, N., and Su, W., 2016. "Modeling of highly flexible multifunctional wings for energy harvesting". *Journal of Aircraft,* **53**(4), pp. 1033–1044.

[9] Hosking, N., and Sotoudeh, Z., 2019. "Comprehensive analysis of smart beams". *AIAA Journal,* **57**(1), pp. 408–420.

[10] Asdaque, P. M. G. B., Banerjee, S., and Roy, S., 2019. "An electromechanically coupled intrinsic, mixed variational formulation for geometrically nonlinear smart composite beam". *Applied Mathematical Modelling,* **65**, Jan., pp. 549–565.

Fig. 11: Vertical displacement at the tip under dead load

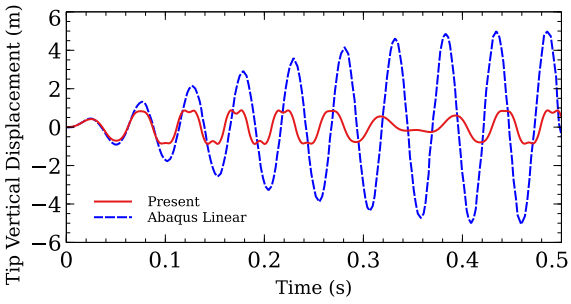

Fig. 12: Voltage harvested at the root element under dead load

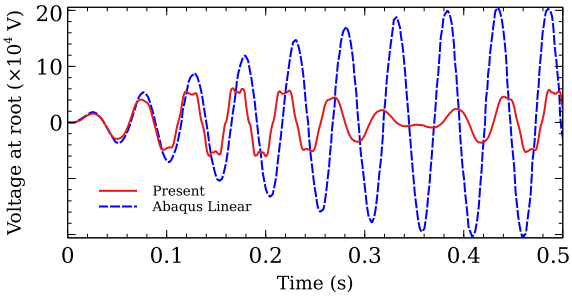

Fig. 13: Axis displacement at the tip under follower load

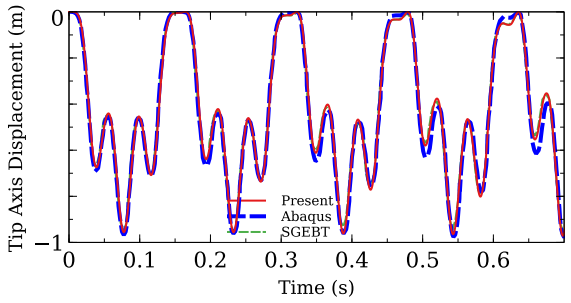

Fig. 14: Vertical displacement at the tip under follower load

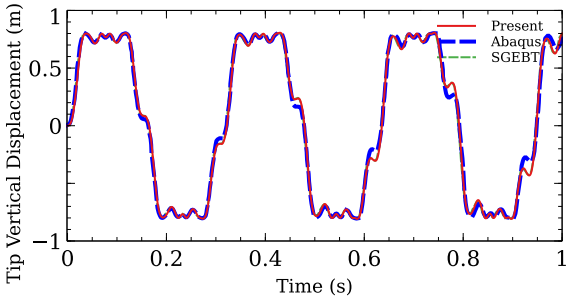

Fig. 15: Voltage harvested at the root element under follower load

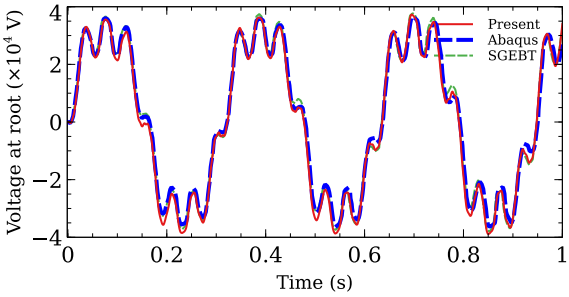

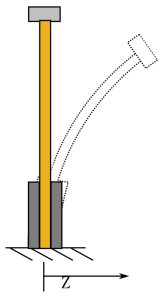

Fig. 16: Schematic representation of bistable verticle beam energy harvester

[11] Asdaque, P. B., and Roy, S., 2019. "Nonlinear dynamic analysis of slender, composite smart-structures under fixed and follower loads". *Composite Structures,* **227**, p. 111269.

[12] Ghiringhelli, G. L., Masarati, P., and Mantegazza, P., 1997. "Characterisation of anisotropic, non-homogeneous beam sections with embedded piezoelectric materials". *Journal of Intelligent Material Systems and Structures,* **8**(10), pp. 842–858.

[13] Roy, S., and Yu, W., 2009. "A coupled timoshenko model for smart slender structures". *International Journal of Solids and Structures,* **46**(13), pp. 2547–2555.

[14] Zhu, W., and Morandini, M., 2020. "Multiphysics cross-section analysis of smart beams". *Mechanics of Advanced Materials and Structures*, pp. 1–18.

[15] Cottone, F., Gammaitoni, L., Vocca, H., Ferrari, M., and Ferrari, V., 2012. "Piezoelectric buckled beams for random vibration energy harvesting". *Smart materials and structures,* **21**(3), p. 035021.

[16] Friswell, M. I., Ali, S. F., Bilgen, O., Adhikari, S., Lees, A. W., and Litak, G., 2012. "Non-linear piezoelectric vibration energy harvesting from a vertical cantilever beam with tip mass". *Journal of Intelligent Material Systems and Structures,* **23**(13), pp. 1505–1521.

[17] Ghiringhelli, G. L., Masarati, P., and Mantegazza, P., 2000. "Multibody implementation of finite volume C^0 beams". *AIAA journal,* **38**(1), pp. 131–138.

[18] Morandini, M., Chierichetti, M., and Mantegazza, P., 2010. "Characteristic behavior of prismatic anisotropic beam via generalized eigenvectors". *International Journal of Solids and Structures,* **47**(10), pp. 1327–1337.

[19] Masarati, P., Lanz, M., and Mantegazza, P., 2001. "Multistep integration of ordinary, stiff and differential-algebraic problems for multibody dinamics applications". In Xvi Congresso Nazionale AIDAA, pp. 1–10.

[20] Masarati, P., Morandini, M., and Mantegazza, P., 2014. "An efficient formulation for general-purpose multi-

body/multiphysics analysis". *Journal of Computational and Nonlinear Dynamics,* **9**(4).

[21] Masarati, P., 2009. "Direct eigenanalysis of constrained system dynamics". *Proceedings of the Institution of Mechanical Engineers, Part K: Journal of Multi-body Dynamics,* **223**(4), pp. 335–342.

[22] Geuzaine, C., and Remacle, J.-F., 2009. "Gmsh: A 3-d finite element mesh generator with built-in pre-and post-processing facilities". *International journal for numerical methods in engineering,* **79**(11), pp. 1309–1331.

[23] Syta, A., Litak, G., Friswell, M. I., and Adhikari, S., 2016. "Multiple solutions and corresponding power output of a nonlinear bistable piezoelectric energy harvester". *The European Physical Journal B,* **89**(4), p. 99.

[24] Li, Y., Zhou, S., Yang, Z., Guo, T., and Mei, X., 2019. "High-performance low-frequency bistable vibration energy harvesting plate with tip mass blocks". *Energy,* **180**, pp. 737–750.

Appendix A: Prediction-Correction approach

The governing equation is described in a mixed differential-algebraic equation (DAE)

$$\boldsymbol{r}(\boldsymbol{y},\dot{\boldsymbol{y}},t)=\boldsymbol{0} \tag{28}$$

A prediction-correction approach is used in the time marching procedure. A implicit A/L stable linear multistep integration scheme proposed by [19, 20] expressed as Eqn. (29) is used first to generate a prediction $\boldsymbol{y}_k^{(0)}$ based on the extrapolated derivative $\dot{\boldsymbol{y}}_k^{(0)}$,

$$\boldsymbol{y}_k=\sum_{i=1,2}\boldsymbol{a}_i\boldsymbol{y}_{k-i}+h\sum_{i=0,2}\boldsymbol{b}_i\dot{\boldsymbol{y}}_{k-i} \tag{29}$$

Where h is the time step. $\boldsymbol{y}_k$, $\dot{\boldsymbol{y}}_k$ are the unknown values and time derivatives at current time t_k. $\boldsymbol{y}_{k-i}$, $\dot{\boldsymbol{y}}_{k-i}$($i$=1, 2) are the values and time derivatives at time t_k-h and t_k-2h respectively, and can be regarded as constants at current time t_k. $\boldsymbol{a}_i$ and $\boldsymbol{b}_i$ are the weight factors. And then according to the perturbation of Eqn. (29)

$$\triangle\boldsymbol{y}_k=h\boldsymbol{b}_0\triangle\dot{\boldsymbol{y}}_k \tag{30}$$

the correction to predicted value can be solved iteratively by using the Newton-Raphson method.

$$(hb_0\boldsymbol{r}_{/\boldsymbol{y}}+\boldsymbol{r}_{/\dot{\boldsymbol{y}}})\triangle\dot{\boldsymbol{y}}_k=-\boldsymbol{r}(\boldsymbol{y}_k^{(j)},\dot{\boldsymbol{y}}_k^{(j)},t_k) \tag{31}$$

$$\dot{\boldsymbol{y}}_k^{(j+1)}=\triangle\dot{\boldsymbol{y}}_k+\dot{\boldsymbol{y}}_k^{(j)} \tag{32}$$

$$\boldsymbol{y}_k^{(j+1)}=hb_0\triangle\dot{\boldsymbol{y}}_k^{(j)}+\boldsymbol{y}_k^{(j)} \tag{33}$$

where j refers to the iterations, $\boldsymbol{r}_{/\boldsymbol{y}}$ and $\boldsymbol{r}_{/\dot{\boldsymbol{y}}}$ are the partial derivatives with respect to $\boldsymbol{y}$ and $\dot{\boldsymbol{y}}$. $hb_0\boldsymbol{r}_{/\boldsymbol{y}}+\boldsymbol{r}_{/\dot{\boldsymbol{y}}}$ forms the Jacobian matrix and $-\boldsymbol{r}(\boldsymbol{y}_k^{(j)},\dot{\boldsymbol{y}}_k^{(j)},t_k)$ is the residual.

Appendix B: Rotation representation

The rotation matrix is handled in a incremental manner, which is updated using the incremental Cayley-Gibbs-Rodrigues rotation parameter $\boldsymbol{g}$,

$$\begin{aligned}\boldsymbol{R}&=\boldsymbol{I}+\frac{4}{4+\boldsymbol{g}^T\boldsymbol{g}}(\boldsymbol{g}\times+\frac{1}{2}\boldsymbol{g}\times\boldsymbol{g}\times)\\&=\boldsymbol{I}+\boldsymbol{G}\boldsymbol{g}\times\end{aligned} \tag{34}$$

$$\boldsymbol{G}=\frac{4}{4+\boldsymbol{g}^T\boldsymbol{g}}(\boldsymbol{I}+\frac{1}{2}\boldsymbol{g}\times) \tag{35}$$

$$\boldsymbol{g}=2\tan(\frac{\theta}{2})\boldsymbol{n} \tag{36}$$

$\boldsymbol{n}$ is the direction of the rotation axis, and θ is the magnitude. An Updated-Updated approach which refers the rotation unknowns $\boldsymbol{g}$ to the predicted configuration at the end of the current time step rather than the corrected configuration at the beginning of the current time step, calculated from the solution at the previous time steps. In this manner, the rotation unknowns represents the corrections with respect to the predicted state, and can be reasonably approximated, for the linearization of the system of nonlinear equations, as small rotations with respect to the predicted orientation [17, 20].

Thus the corrected orientation is $\boldsymbol{R}=\boldsymbol{R}_\delta\boldsymbol{R}_r$, $\boldsymbol{R}_r$ is the predicted rotation, $\boldsymbol{R}_\delta$ is the variation of rotation matrix from the predicted one at the beginning of the current time step. The angular velocity and curvature at current time step can be expressed as:

$$\begin{aligned}\boldsymbol{\omega}&=\dot{\boldsymbol{R}}_\delta\boldsymbol{R}_\delta^T+\boldsymbol{R}_\delta\dot{\boldsymbol{R}}_r\boldsymbol{R}_r\boldsymbol{R}_\delta^T\\&=\boldsymbol{\omega}_\delta+\boldsymbol{R}_\delta\boldsymbol{\omega}_r=\boldsymbol{G}\dot{\boldsymbol{g}}+\boldsymbol{R}_\delta\boldsymbol{\omega}_r\end{aligned} \tag{37}$$

$$\boldsymbol{\kappa}=\boldsymbol{\kappa}_\delta+\boldsymbol{R}_\delta\boldsymbol{\kappa}_r=\boldsymbol{G}\boldsymbol{g}'+\boldsymbol{R}_\delta\boldsymbol{\kappa}_r \tag{38}$$

$$\boldsymbol{R}_\delta=\boldsymbol{G}\boldsymbol{g}_\delta\times \tag{39}$$

where $\boldsymbol{\omega}_\delta$ and $\boldsymbol{\kappa}_\delta$ are angular velocity and curvature pertubations with respect to the predicted one.

Appendix C: Linerazition of circuit equation

The solution requires to linearize Eqn. (20) with respect to the predicted phase. The linearization of the first equilibrium equation in Eqn. (21) has already been discussed in [17]. The only modification lies in the constitutive law, the stiffness matrix of fully coupled electromechanical constitutive law is shaped as a $(6+N)\times(6+N)$ matrix, N is the number of electrode pairs, rather than a 6×6 matrix in classical constitutive law(without piezoelectric materials). Thus the contribution of external electric potentials to internal forces should be taken into account. Here we only focus on the circuit equation of Eqn. (21).

The unknowns are the nodal displacements $\boldsymbol{x}$, rotation parameters $\boldsymbol{g}$ and voltage differences at electrode pairs $\boldsymbol{V}$. The linearized circuit equation at element level can be written as:

$$\sum_{\alpha=I,II}\begin{pmatrix}\boldsymbol{K}_{\varepsilon}\triangle\dot{\tilde{\boldsymbol{\varepsilon}}}_{\alpha}+\boldsymbol{K}_{\kappa}\triangle\dot{\tilde{\boldsymbol{\kappa}}}_{\alpha}+\boldsymbol{C}_{p}\triangle\dot{V}_{\alpha}\\ +\boldsymbol{K}_{\varepsilon}\dot{\tilde{\boldsymbol{\varepsilon}}}_{\alpha}+\boldsymbol{K}_{\kappa}\dot{\tilde{\boldsymbol{\kappa}}}_{\alpha}+\boldsymbol{C}_{p}\dot{V}_{\alpha}\end{pmatrix}=-\frac{V_p}{R} \tag{40}$$

Here α= I, II is the evaluation point index, $\Delta(\cdot)$ refers to the perturbation with respect to predicted phase which expressed with a subscript $(\cdot)_r$. The corresponding relations are linearized around the predicted configuration, thus assuming $\boldsymbol{g}=\dot{\boldsymbol{g}}=\boldsymbol{0}$ and dropping any term that is at least linear with respect to either $\boldsymbol{g}$ of $\dot{\boldsymbol{g}}$.

$$\begin{aligned}\triangle\boldsymbol{\omega}_{\alpha}&=\triangle(\boldsymbol{G}\dot{\boldsymbol{g}})+\triangle\boldsymbol{R}\boldsymbol{\omega}_r\\&=\boldsymbol{G}\triangle\dot{\boldsymbol{g}}+(\boldsymbol{G}\triangle\boldsymbol{g})\times\boldsymbol{\omega}_r\\&=\triangle\dot{\boldsymbol{g}}+\triangle\boldsymbol{g}\times\boldsymbol{\omega}_r\\&=N_{\alpha i}\triangle\dot{\boldsymbol{g}}_i-\boldsymbol{\omega}_{r\alpha}\times N_{\alpha i}\triangle\boldsymbol{g}_i\end{aligned} \tag{41}$$

$$\begin{aligned}\triangle\boldsymbol{R}_{\alpha}&=\triangle\boldsymbol{g}\times\boldsymbol{R}_r\\&=N_{\alpha i}\triangle\boldsymbol{g}_i\times\boldsymbol{R}_r\\&=N_{\alpha i}\triangle\boldsymbol{g}_i\times\boldsymbol{R}_r\end{aligned} \tag{42}$$

$$\begin{aligned}\triangle\boldsymbol{R}_{\alpha}^{T}&=-\boldsymbol{R}_r^{T}\triangle\boldsymbol{g}\times\\&=-(\boldsymbol{R}_{r\alpha}^{T}N_{\alpha i}\triangle\boldsymbol{g}_i)\times\end{aligned} \tag{43}$$

$$\triangle\boldsymbol{l}_{\alpha}=\triangle\boldsymbol{p}'=N'_{\alpha i}(\triangle\boldsymbol{x}_i+\triangle\boldsymbol{R}_{\alpha}\tilde{\boldsymbol{f}}_i) \tag{44}$$

$$=N'_{\alpha i}(\triangle\boldsymbol{x}_i-(\boldsymbol{R}_i\tilde{\boldsymbol{f}}_i)\times\triangle\boldsymbol{g}_i) \tag{45}$$

$$\dot{\boldsymbol{R}}=\boldsymbol{\omega}\times\boldsymbol{R} \tag{46}$$

$$\begin{aligned}\triangle\dot{\boldsymbol{R}}_{\alpha}&=\triangle\boldsymbol{\omega}\times\boldsymbol{R}+\boldsymbol{\omega}\times\triangle\boldsymbol{R}\\&=\triangle\dot{\boldsymbol{g}}\times\boldsymbol{R}-\boldsymbol{\omega}_r\times\triangle\boldsymbol{g}\times\boldsymbol{R}+\boldsymbol{\omega}\times\triangle\boldsymbol{g}\times\boldsymbol{R}_r\\&=N_{\alpha i}\triangle\dot{\boldsymbol{g}}_i\times\boldsymbol{R}_i-\boldsymbol{\omega}_{ri}\times N_{\alpha i}\triangle\boldsymbol{g}_i\times\boldsymbol{R}_i\\&\quad+\boldsymbol{\omega}_i\times N_{\alpha i}\triangle\boldsymbol{g}_i\times\boldsymbol{R}_{ri}\end{aligned} \tag{47}$$

$$\begin{aligned}&=(N_{\alpha i}\triangle\dot{\boldsymbol{g}}_i-\boldsymbol{\omega}_{ri}\times N_{\alpha i}\triangle\boldsymbol{g}_i)\times\boldsymbol{R}_i\\&\quad+\boldsymbol{\omega}_i\times N_{\alpha i}\triangle\boldsymbol{g}_i\times\boldsymbol{R}_{ri}\end{aligned} \tag{48}$$

$$\begin{aligned}&=N_{\alpha i}\triangle\dot{\boldsymbol{g}}_i\times\boldsymbol{R}_i-N_{\alpha i}\triangle\boldsymbol{g}_i\otimes\boldsymbol{\omega}_{ri}\boldsymbol{R}_i\\&\quad+\boldsymbol{\omega}_{ri}\otimes N_{\alpha i}\triangle\boldsymbol{g}_i\boldsymbol{R}_i+\boldsymbol{\omega}_i\times N_{\alpha i}\triangle\boldsymbol{g}_i\times\boldsymbol{R}_{ri}\end{aligned} \tag{49}$$

$$\begin{aligned}\triangle\dot{\boldsymbol{l}}_{\alpha}&=N'_{\alpha i}\boldsymbol{p}_i=N'_{\alpha i}(\triangle\dot{\boldsymbol{x}}_i+\triangle\dot{\boldsymbol{R}}_i\tilde{\boldsymbol{f}}_i)\\&=N'_{\alpha i}\triangle\dot{\boldsymbol{x}}_i\\&\quad+N'_{\alpha i}\begin{pmatrix}\triangle\dot{\boldsymbol{g}}_i\times\boldsymbol{R}_i-\triangle\boldsymbol{g}_i\otimes\boldsymbol{\omega}_{ri}\boldsymbol{R}_i\\+\boldsymbol{\omega}_r\otimes\boldsymbol{R}_i^{T}\triangle\boldsymbol{g}_i+\boldsymbol{\omega}_i\times\triangle\boldsymbol{g}_i\times\boldsymbol{R}_{ri}\end{pmatrix}\tilde{\boldsymbol{f}}_i\\&=N'_{\alpha i}(\triangle\dot{\boldsymbol{x}}_i-(\boldsymbol{R}_i\tilde{\boldsymbol{f}}_i)\times\triangle\dot{\boldsymbol{g}}_i-(\boldsymbol{\omega}_{ri}\boldsymbol{R}_i\tilde{\boldsymbol{f}}_i)\triangle\boldsymbol{g}_i\\&\quad+\boldsymbol{\omega}_{ri}\otimes(\boldsymbol{R}_i^{T}\tilde{\boldsymbol{f}}_i)\triangle\boldsymbol{g}_i-\boldsymbol{\omega}_i\times(\boldsymbol{R}_{ri}\tilde{\boldsymbol{f}}_i)\times\triangle\boldsymbol{g}_i)\end{aligned} \tag{50}$$

$$\begin{aligned}\triangle\dot{\tilde{\boldsymbol{\varepsilon}}}_{\alpha}&=\triangle\boldsymbol{R}^{T}(\dot{\boldsymbol{l}}-\boldsymbol{\omega}\times\boldsymbol{l})+\boldsymbol{R}^{T}(\triangle\dot{\boldsymbol{l}}-\triangle\boldsymbol{\omega}\times\boldsymbol{l}-\boldsymbol{\omega}\times\triangle\boldsymbol{l})\\&=\boldsymbol{R}_{r\alpha}^{T}(\dot{\boldsymbol{l}}_{\alpha}-\boldsymbol{\omega}_{\alpha}\times\boldsymbol{l}_{\alpha})\times N_{\alpha i}\triangle\boldsymbol{g}_i\\&\quad+\boldsymbol{R}_{\alpha}^{T}N'_{\alpha i}(\triangle\dot{\boldsymbol{x}}_i-(\boldsymbol{R}_i\tilde{\boldsymbol{f}}_i)\times\triangle\dot{\boldsymbol{g}}_i)\\&\quad-\boldsymbol{R}_{\alpha}^{T}N'_{\alpha i}(\boldsymbol{\omega}_{ri}\boldsymbol{R}_i\tilde{\boldsymbol{f}}_i)\triangle\boldsymbol{g}_i+\boldsymbol{R}_{\alpha}^{T}N'_{\alpha i}\boldsymbol{\omega}_{ri}\otimes(\boldsymbol{R}_i^{T}\tilde{\boldsymbol{f}}_i)\triangle\boldsymbol{g}_i\\&\quad-\boldsymbol{R}_{\alpha}^{T}N'_{\alpha i}\boldsymbol{\omega}_i\times(\boldsymbol{R}_{ri}\tilde{\boldsymbol{f}}_i)\times\triangle\boldsymbol{g}_i\\&\quad+\boldsymbol{R}_{\alpha}^{T}\boldsymbol{l}_{\alpha}\times N_{\alpha i}\triangle\dot{\boldsymbol{g}}_i-\boldsymbol{R}_{\alpha}^{T}\boldsymbol{\omega}_{\alpha}\times N_{\alpha i}\triangle\boldsymbol{g}_i\times\boldsymbol{l}_{\alpha}\\&\quad-\boldsymbol{R}_{\alpha}^{T}\boldsymbol{\omega}_{\alpha}\times N'_{\alpha i}(\triangle\boldsymbol{x}_i-(\boldsymbol{R}_i\tilde{\boldsymbol{f}}_i)\times\triangle\boldsymbol{g}_i)\\&=\boldsymbol{R}_{r\alpha}^{T}(\dot{\boldsymbol{l}}_{\alpha}-\boldsymbol{\omega}_{\alpha}\times\boldsymbol{l}_{\alpha})\times N_{\alpha i}\triangle\boldsymbol{g}_i\\&\quad+\boldsymbol{R}_{\alpha}^{T}N'_{\alpha i}(\triangle\dot{\boldsymbol{x}}_i-(\boldsymbol{R}_i\tilde{\boldsymbol{f}}_i)\times\triangle\dot{\boldsymbol{g}}_i)\\&\quad-\boldsymbol{R}_{\alpha}^{T}N'_{\alpha i}(\boldsymbol{\omega}_{ri}\boldsymbol{R}_i\tilde{\boldsymbol{f}}_i)\triangle\boldsymbol{g}_i+\boldsymbol{R}_{\alpha}^{T}N'_{\alpha i}\boldsymbol{\omega}_{ri}\otimes(\boldsymbol{R}_i^{T}\tilde{\boldsymbol{f}}_i)\triangle\boldsymbol{g}_i\\&\quad-\boldsymbol{R}_{\alpha}^{T}N'_{\alpha i}\boldsymbol{\omega}_i\times(\boldsymbol{R}_{ri}\tilde{\boldsymbol{f}}_i)\times\triangle\boldsymbol{g}_i\\&\quad+\boldsymbol{R}_{\alpha}^{T}\boldsymbol{l}_{\alpha}\times N_{\alpha i}\triangle\dot{\boldsymbol{g}}_i+(\boldsymbol{\omega}_{\alpha}\cdot\boldsymbol{l}_{\alpha})\boldsymbol{R}_{\alpha}^{T}N_{\alpha i}\triangle\boldsymbol{g}_i\\&\quad-\boldsymbol{R}_{\alpha}^{T}\boldsymbol{\omega}_{\alpha}\otimes\boldsymbol{l}_{\alpha}\cdot N_{\alpha i}\triangle\boldsymbol{g}_i\\&\quad-\boldsymbol{R}_{\alpha}^{T}\boldsymbol{\omega}_{\alpha}\times N'_{\alpha i}(\triangle\boldsymbol{x}_i-(\boldsymbol{R}_i\tilde{\boldsymbol{f}}_i)\times\triangle\boldsymbol{g}_i)\end{aligned} \tag{51}$$

$$\begin{aligned}\triangle\dot{\tilde{\boldsymbol{\kappa}}}_{\alpha}&=\triangle\boldsymbol{R}_{\alpha}^{T}(\boldsymbol{G}\dot{\boldsymbol{g}}'-\boldsymbol{\omega}_{\alpha}\times\boldsymbol{G}\boldsymbol{g}')\\&\quad+\boldsymbol{R}_{\alpha}^{T}\begin{pmatrix}\triangle\boldsymbol{G}\dot{\boldsymbol{g}}'+\boldsymbol{G}\triangle\dot{\boldsymbol{g}}'-\triangle\boldsymbol{\omega}_{\alpha}\times\boldsymbol{G}\boldsymbol{g}'\\+\Delta\dot{\boldsymbol{G}}\boldsymbol{g}'-\boldsymbol{\omega}_{\alpha}\times\triangle\boldsymbol{G}\boldsymbol{g}'-\boldsymbol{\omega}_{\alpha}\times\boldsymbol{G}\triangle\boldsymbol{g}'\end{pmatrix}\\&=\triangle\boldsymbol{R}_{\alpha}^{T}(\boldsymbol{G}N'_{\alpha i}\dot{\boldsymbol{g}}_i-\boldsymbol{\omega}_{\alpha}\times\boldsymbol{G}N'_{\alpha i}\boldsymbol{g}_i)\\&\quad+\boldsymbol{R}_{\alpha}^{T}\begin{pmatrix}\triangle\boldsymbol{G}N'_{\alpha i}\dot{\boldsymbol{g}}_i+\boldsymbol{G}N'_{\alpha i}\triangle\dot{\boldsymbol{g}}_i\\-\triangle\boldsymbol{\omega}_{\alpha}\times\boldsymbol{G}N'_{\alpha i}\boldsymbol{g}_i+\Delta\dot{\boldsymbol{G}}N'_{\alpha i}\boldsymbol{g}_i\\-\boldsymbol{\omega}_{\alpha}\times\triangle\boldsymbol{G}N'_{\alpha i}\triangle\boldsymbol{g}_i-\boldsymbol{\omega}_{\alpha}\times\boldsymbol{G}N'_{\alpha i}\triangle\boldsymbol{g}_i\end{pmatrix}\\&=\boldsymbol{R}_{\alpha}^{T}(\boldsymbol{G}N'_{\alpha i}\triangle\dot{\boldsymbol{g}}_i-\boldsymbol{\omega}_{\alpha}\times\boldsymbol{G}N'_{\alpha i}\triangle\boldsymbol{g}_i)\\&=\boldsymbol{R}_{\alpha}^{T}N'_{\alpha i}\triangle\dot{\boldsymbol{g}}_i-\boldsymbol{R}_{\alpha}^{T}\boldsymbol{\omega}_{\alpha}\times N'_{\alpha i}\triangle\boldsymbol{g}_i\end{aligned} \tag{52}$$

According to Eqn. (30), the perturbation of unknown state variables can be expressed in terms of its time derivative in correction phase

$$\begin{aligned} \triangle \boldsymbol{x}_i &= hb_0 \triangle \dot{\boldsymbol{x}}_i \\ \triangle \boldsymbol{g}_i &= hb_0 \triangle \dot{\boldsymbol{g}}_i \\ \triangle \boldsymbol{V} &= hb_0 \triangle \dot{\boldsymbol{V}} \end{aligned} \tag{53}$$

Substituting Eqn. (25)(26)(51)(52) and Eqn. (53) into Eqn. (40), yields the Jacobian matrix, and finally the time marching solution can be solved iteratively by using Newton-Raphson method.

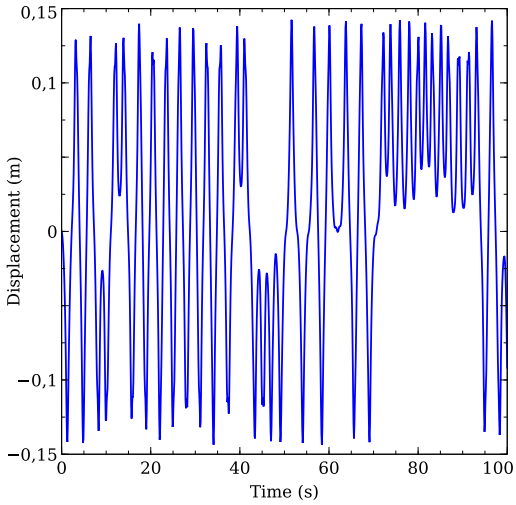

(a) Displacement

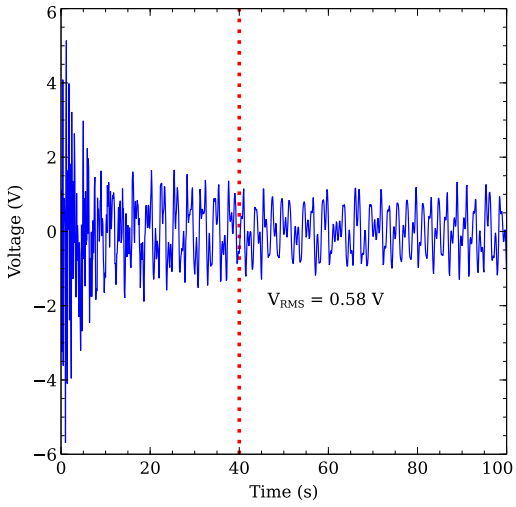

(b) Voltage

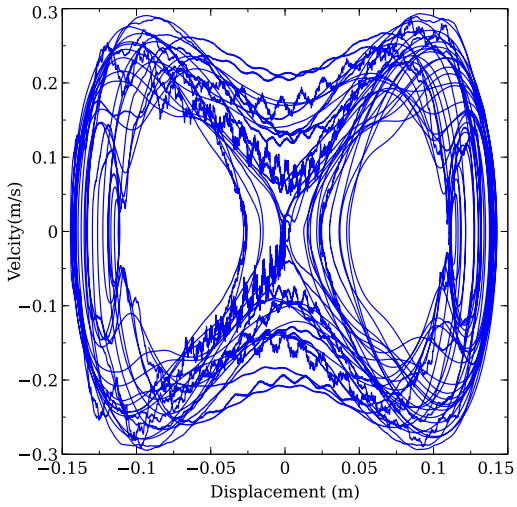

(c) Displacement-velocity

Fig. 17: Bistable beam response under low amplitude excitation ($z = 18.5$ mm, $f = 1.4$ Hz)

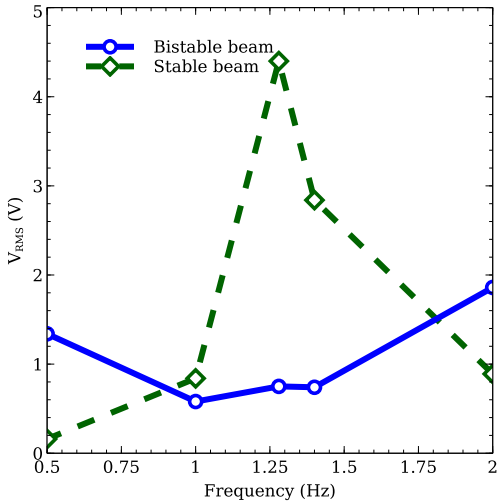

Fig. 18: Voltage RMS as a function of the excitation frequency for both the bistable and the stable beam